

1 INTRODUCTION

2 Above Earth's atmosphere are the Van Allen radiation belts, a toroidally-shaped
3 pair of belts that consist of a complex and dynamic plasma environment. The inner
4 radiation belt consists of mostly energetic protons, is very stable on year time scales,
5 and is located within 2 Earth radii (measured near the equator) above Earth's Earth's
6 surface. The outer radiation belt, on the other hand, consists of mostly energetic
7 electrons, is highly dynamic on day, and even hour time scales, and is typically
8 found between 4 and 8 Earth radii above Earth's surface. The radiation belts pose a
9 challenge to space exploration due to their effects on our technology-driven society.
10 Some of the effects include: a higher radiation dose for astronauts and cosmonauts,
11 degradation of silicon to the point where transistors malfunction, computer memory
12 corrupts due to bit flips, etc. With these effects in mind, it is no surprise that the
13 radiation belts have been extensively studied since their discovery in the 1960s.

14 The radiation belt plasma is at times unstable which in turn generate electric and
15 magnetic waves. These waves in turn accelerate and scatter radiation belt particles
16 with a variety of wave-particle mechanisms. One form of wave-particle interactions
17 scatter particles into Earth's atmosphere in the form of electron microbursts.

18 Electron microbursts, henceforth referred to as microbursts, are typically
19 observed by low Earth orbiting spacecraft, sounding rockets, and high altitude
20 balloons as a sub-second impulse of electrons. Some of the most intense microbursts
21 have electron fluxes that are a factor of 10 to 100 above the background (for example
22 see Fig. 7 in Blake et al. (1996)). Since they were first reported by Anderson and
23 Milton (1964), the intense transient nature of microbursts have compelled countless
24 researchers to understand their properties, their effects on the environment, and the
25 physical mechanism(s) that create microbursts. Microbursts are widely believed

26 to be created by wave-particle scattering between a plasma wave called whistler
 27 mode chorus and outer radiation belt electrons, although many details regarding the
 28 scattering mechanism are unconstrained or unknown. The goal of this dissertation is
 29 to study the wave-particle scattering mechanism that scatters electron microbursts.

30 This chapter serves as an introduction to the fundamental physical concepts
 31 that are essential to understand wave-particle interactions in Earth's magnetosphere.
 32 We will first derive the motion of individual charged particles in Earth's electric and
 33 magnetic fields. Next we will cover how various groups of charged particles coalesce
 34 to form the major particle populations in the magnetosphere. Then, we will cover
 35 the various mechanisms that accelerate and scatter particles in the magnetosphere.
 36 Lastly, we will review the basics of microbursts as a jumping-off point for the rest of
 37 the dissertation.

38 Charged Particle Motion in Electric and Magnetic Fields

A charged particle trapped in the magnetosphere will experience three types of periodic motion in Earth's nearly dipolar magnetic field. The three motions are ultimately due to the Lorentz force that a particle of momentum \vec{p} , charge q , and velocity \vec{v} experiences in an electric field \vec{E} and magnetic field \vec{B} and is given by

$$\frac{d\vec{p}}{dt} = q(\vec{E} + \vec{v} \times \vec{B}). \quad (1.1)$$

39 In the magnetosphere, the three periodic motions, in decreasing frequency, are
 40 gyration, bounce, and drift and are schematically shown in Fig. 1.1. Each periodic
 41 motion has a corresponding conserved quantity i.e. an adiabatic invariant.

The highest frequency periodic motion is gyration about a magnetic field of

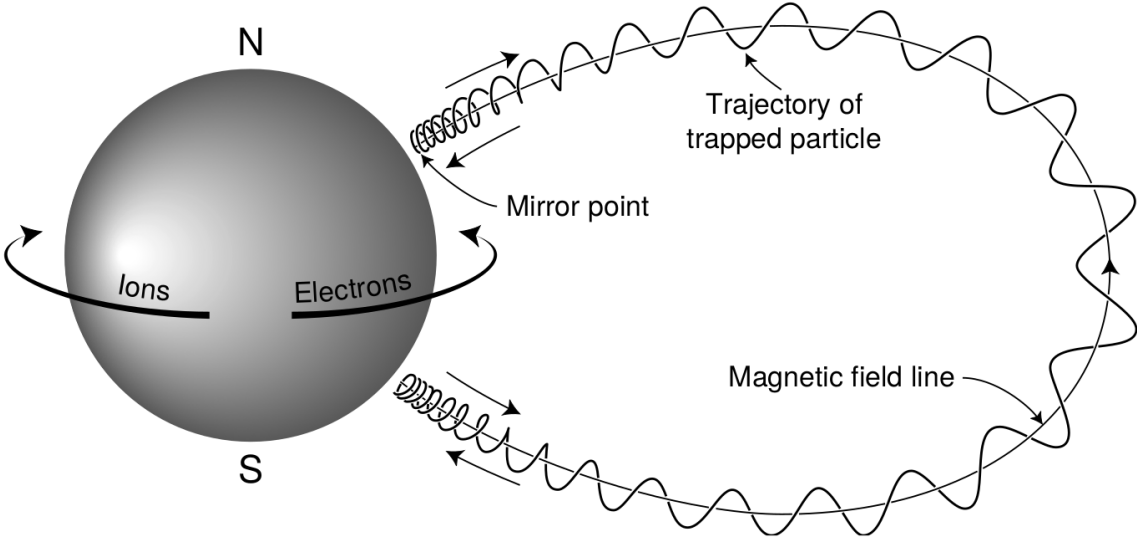


Figure 1.1: The three periodic motions of charged particles in Earth's dipole magnetic field. These motions are: gyration about the magnetic field line, bounce motion between the magnetic poles, and azimuthal drift around the Earth. Figure from (Baumjohann and Treumann, 1997).

magnitude B . This motion is circular with a Larmor radius of

$$r = \frac{mv_{\perp}}{|q|B} \quad (1.2)$$

where m is the mass and v_{\perp} the particle's velocity perpendicular to \vec{B} . This motion has a corresponding gyrofrequency

$$\Omega = \frac{|q|B}{m} \quad (1.3)$$

in units of radians/second. In the radiation belts, the electron gyrofrequency, Ω_e is on the order of a kHz. The corresponding adiabatic invariant is found by integrating the particle's canonical momentum around the particle's path of gyration

$$J_i = \oint (\vec{p} + q\vec{A}) \cdot d\vec{l} \quad (1.4)$$

42 where J_i is the i^{th} adiabatic invariant and \vec{A} is the magnetic vector potential. This
 43 integral is carried out by integrating the first term over the circumference of the
 44 gyro orbit and integrating the second term using Stokes theorem to calculate the
 45 magnetic flux enclosed by the gyro orbit. The gyration invariant is $J_1 \sim v_\perp^2/B$, which
 46 is conserved when the frequency, ω of a force acting on the gyrating electron satisfies
 47 $\omega \ll \Omega_e$.

48 The second highest frequency periodic motion is bouncing due to a parallel
 49 gradient in \vec{B} . This periodic motion naturally arises in the magnetosphere because
 50 Earth's magnetic field is stronger near the poles, and artificially in the laboratory
 51 in magnetic bottle machines. To understand this motion we first we need to define
 52 the concept of pitch angle, α as the angle between \vec{B} and \vec{v} which is schematically
 53 shown in Fig. 1.2a. The pitch angle relates v with v_\perp , and $v_{||}$ (the component of the
 54 particles velocity parallel to \vec{B}). As shown in Fig. 1.2b and 1.2c, a smaller (larger)
 55 α will increase (decrease) the distance that the charged particle travels parallel to \vec{B} ,
 56 during one gyration.

Assuming the particle's kinetic energy is conserved, the conservation of J_1
 implies that given a particle's $v_\perp(0)$ and $B(0)$ at the magnetic equator (where
 Earth's magnetic field is usually at a minimum), we can calculate its $v_\perp(s)$ along the
 particle's path s by calculating $B(s)$ from magnetic field models. Thus the particle's
 perpendicular velocity is then related via

$$\frac{v_\perp^2(0)}{B(0)} = \frac{v_\perp^2(s)}{B(s)} \quad (1.5)$$

57 which can be rewritten as

$$\frac{v^2 \sin^2 \alpha(0)}{B(0)} = \frac{v^2 - v_{||}^2(s)}{B(s)} \quad (1.6)$$

⁵⁸ and re-arranged to solve for $v_{||}(s)$

$$v_{||}(s) = v \sqrt{1 - \frac{B(s)}{B(0)} \sin^2 \alpha(0)} \quad (1.7)$$

⁵⁹ which will tend towards 0 when the second term in the radical approaches 1.

⁶⁰ The location where $v_{||}(s) = 0$ is called the mirror point and is where a particle
⁶¹ reverses direction. Since Earth's magnetic field is stronger towards the poles, the
⁶² mirroring particle will execute periodic bounce motion between its two mirror points
⁶³ in the northern and southern hemispheres. The corresponding adiabatic invariant, J_2
⁶⁴ is

$$J_2 = \oint p_{||} ds \quad (1.8)$$

where ds describes the particle path between the mirror points in the northern and southern hemispheres (see Fig. 1.1). J_2 is found by substituting Eq. 1.7 into Eq. 1.8 and defining the magnetic field strength at the mirror points as B_m (where $\alpha(m) = 90^\circ$). The J_2 integral can be written as

$$J_2 = 2p \int_{m_n}^{m_s} \sqrt{1 - \frac{B(s)}{B(m)}} ds \quad (1.9)$$

⁶⁵ where m_n and m_s are the northern and southern mirror points, respectively. The
⁶⁶ bounce period can be estimated (e.g. Baumjohann and Treumann, 1997) to be

$$t_b \approx \frac{LR_e}{\sqrt{W/m}} (3.7 - 1.6 \sin \alpha(0)) \quad (1.10)$$

⁶⁷ where W is the particle's kinetic energy, and L is the L -shell. L -shell describes the
⁶⁸ distance from the Earth's center to the location where a particular magnetic field
⁶⁹ line crosses the magnetic equator, in units of Earth radii, R_e . As with gyration, the

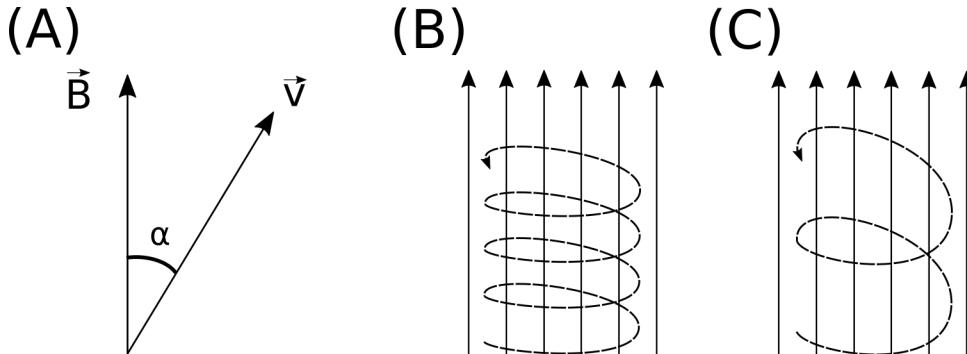


Figure 1.2: Charged particle motion in a uniform magnetic field \vec{B} . Panel (A) shows the geometry defining the pitch angle, α . Panel (B) and (C) show two helical electron trajectories with dashed lines assuming a large and small α (corresponding to a small and large parallel velocity $v_{||}$), respectively.

70 particle will bounce between the mirror points as long as $\omega \ll \Omega_b$, where Ω_b is the
71 bounce frequency.

72 At this stage it is instructional to introduce the notion of the loss cone pitch
73 angle, α_L . A particle with $\alpha \leq \alpha_L$ will mirror at or below ≈ 100 km altitude in
74 the atmosphere. A charged particle gyrating at those altitudes will encounter and
75 Coulomb scatter with the dense atmosphere and be lost from the magnetosphere.

76 The slowest periodic motion experienced by charged particles in Earth's mag-
77 netic field is azimuthal drift around the Earth. This drift results from a combination of
78 a radial gradient in \vec{B} and the curvature of the magnetic field. The radial gradient drift
79 arises because Earth's magnetic field is stronger near the Earth where the particle's
80 gyroradius radius of curvature shrinks as it gyrates towards stronger magnetic field,
81 and expands when it gyrates outward. The overall effect is the particle gyro orbit does
82 not close on itself and negatively charged particles drift east and positively charged
83 particles drift west. The radial gradient drift is further enhanced by the centrifugal
84 force that a particle experiences as it bounces along the curved field lines. The drift
85 adiabatic invariant, J_3 is found by integrating Eq. 1.4 over the complete particle orbit

86 around the Earth. The shape of this drift orbit is known as a drift shell. For J_3 , the
 87 first term is negligible and the second term is the magnetic flux enclosed by the drift
 88 shell, Φ_m i.e. $J_3 \sim \Phi_m$.

89 Figure 1.3 from Schulz and Lanzerotti (1974) shows contours of the gyration,
 90 bounce, and drift frequencies for electrons and protons in Earth's dipole magnetic
 91 field.

Up until now we have considered the three periodic motions due Earth's magnetic field in the absence of electric fields. If \vec{E} is present, a particle's center of gyration i.e., averaged position of the particle over a gyration, will drift with a velocity perpendicular to both \vec{E} and \vec{B} . The drift velocity can be solved using Eq. 1.1 and is

$$\vec{v}_E = \frac{\vec{E} \times \vec{B}}{B^2}. \quad (1.11)$$

92 For more detailed derivations of these motions, see the following texts: Baumjohann
 93 and Treumann (1997); Schulz and Lanzerotti (1974); Tsurutani and Lakhina (1997).

94 Particle Populations and Their Interractions in the Magnetosphere

95 Now that we have looked at the dynamics of single-particle motion in electric
 96 and magnetic fields, we will briefly tour the various macroscopic populations in the
 97 magnetosphere that are illustrated in Fig. 1.4.

98 The sun and its solar wind are ultimately the source of energy input into the
 99 magnetosphere. The solar wind at Earth's orbit is a plasma traveling at supersonic
 100 speeds with an embedded interplanetary magnetic field (IMF). When the solar wind
 101 encounters Earth's magnetic field, the plasma can not easily penetrate into the
 102 magnetosphere because the plasma is frozen-in on magnetic field lines. Thus the
 103 plasma and its magnetic field drapes around the magnetosphere forming a cavity in

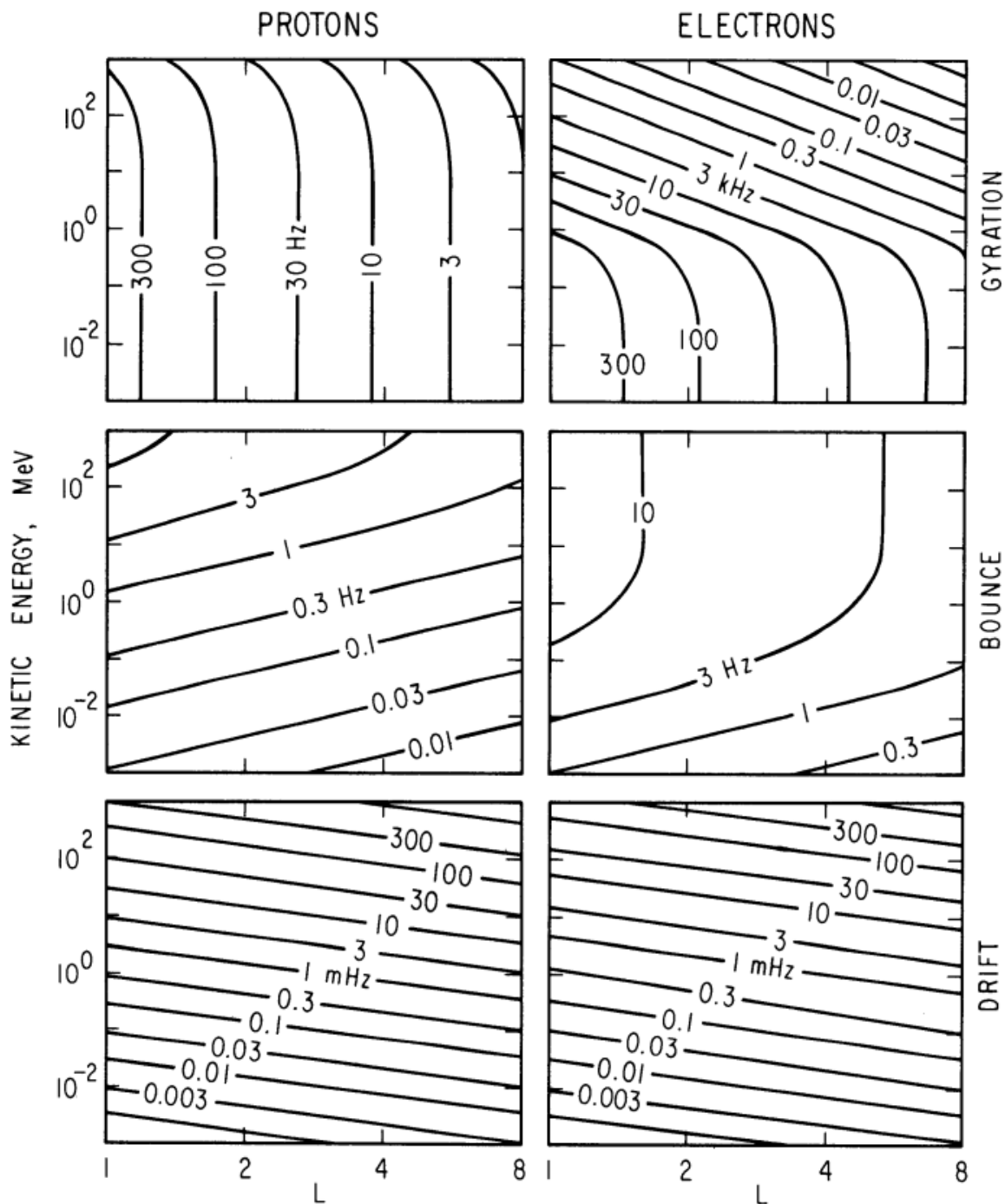


Figure 1.3: Contours of constant gyration, bounce, and drift frequencies for electrons and protons in a dipole field. Figure from Schulz and Lanzerotti (1974).

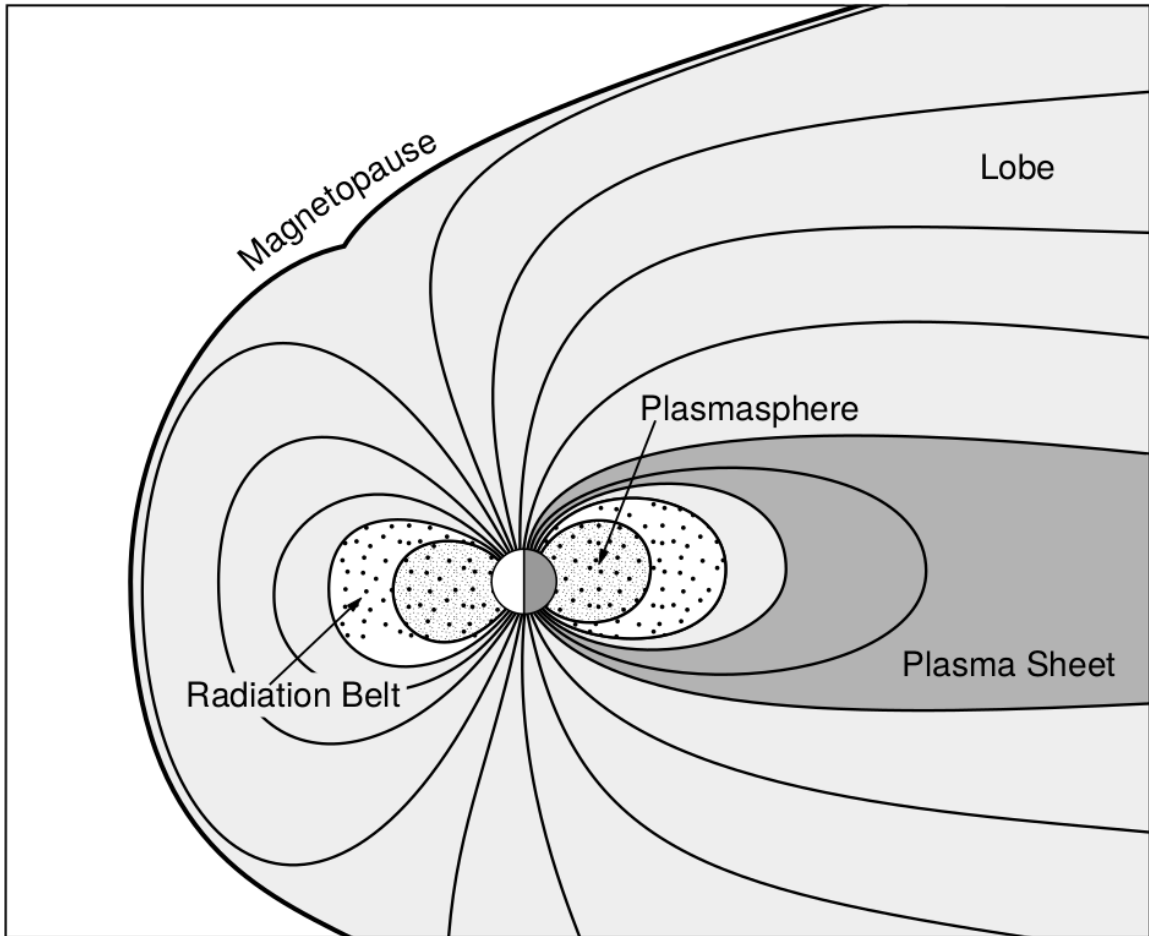


Figure 1.4: Macroscopic structures in the inner magnetosphere most relevant to this dissertation. The plasmasphere, and the radiation belts are shown and ring current is co-located there as well. Figure from Baumjohann and Treumann (1997).

104 the solar wind that is roughly shaped as shown in Fig. 1.4. Because the solar wind
 105 is supersonic at 1 AU, a bow shock exists upstream of the magnetosphere. The solar
 106 wind plasma, after it is shocked by the bow shock, flows around the magnetosphere
 107 inside the magnetosheath. The surface where the solar wind ram pressure and Earth's
 108 magnetic pressure balance is termed the magnetopause, which can be thought of as
 109 a boundary between the solar wind's and Earth's plasma environments. This is
 110 a slightly naive description of the magnetopause, but is nonetheless an instructive
 111 conceptual picture. The shocked plasma then flows past the Earth where it shapes
 112 the magnetotail. In the magnetotail the solar wind magnetic pressure balances Earth's
 113 magnetic field pressure in the lobes. The magnetotail extends on the order of 100
 114 R_E downstream of Earth, and the tailward stretching of magnetic field lines creates
 115 the plasma sheet which exists in the region of low magnetic field strength near the
 116 magnetic equator (e.g. Eastwood et al., 2015).

117 Populations in the Inner Magnetosphere

118 Closer to Earth, where the magnetic field is largely dipolar, are three plasma
 119 populations that comprise the inner magnetosphere: the plasmasphere, the ring
 120 current, and the radiation belts. Before we describe these three particle populations
 121 in detail, we will first introduce the coordinate system that most naturally describes
 122 the inner magnetosphere environment, and the electric fields that affect mostly low
 123 energy particles.

124 In this coordinate system the “radial” coordinate was defined in section 1 and
 125 is the L shell. The azimuthal coordinate is the magnetic local time (MLT). For an
 126 observer above Earth's north pole looking down, MLT is defined to be 0 (midnight)
 127 in the anti-sunward direction, and increases in the counter-clockwise direction with 6
 128 at dawn, 12 at noon (sunward direction), and 18 in dusk. The final coordinate is the

129 magnetic latitude, λ which is analogous to the latitude coordinate in the spherical
 130 coordinate system, and is defined to be 0 at the magnetic equator. This coordinate
 131 system naturally describes the following inner magnetosphere populations.

132 The low energy particle dynamics in the inner magnetosphere are organized by
 133 two electric fields: the co-rotation and the dawn-dusk electric fields. The co-rotation
 134 electric field arises from the rotation of Earth's magnetic field. Since particles are
 135 frozen on magnetic field lines and the plasma conductivity is effectively infinite, to a
 136 non-rotating observer, Earth's rotation appears as a radial electric field that drops off
 137 as $\sim L^2$. This electric field makes particles orbit around the Earth due to the $\vec{E} \times \vec{B}$
 138 drift. The other electric field, pointing from dawn to dusk is called the convection
 139 electric field and is due to the Earthward transport of particles from the magnetotail
 140 that appears as an electric field to a stationary observer (with respect to Earth). The
 141 superposition of the co-rotation and convection electric fields results in a potential
 142 field shown in Fig. 1.5. The shaded area in Fig. 1.5 shows the orbits on which low
 143 energy electrons are trapped, and outside are the untrapped particles. The dynamic
 144 topology of the shaded region in Fig. 1.5 is controlled by only the convection electric
 145 field which is dependent on the solar wind speed and the IMF. The lowest energy
 146 particles, that are most effected by these electric fields, make up the plasmasphere.

147 Plasmasphere The plasmasphere is a dense ($n_e \sim 10^3/\text{cm}^3$), cool plasma
 148 ($\sim \text{eV}$) that extends to $L \sim 4$ (extent is highly dependent on the solar wind and
 149 magnetospheric conditions) and is sourced from the ionosphere. The two main
 150 mechanisms that source the cold plasma from the ionosphere are ultraviolet ionization
 151 by sunlight and particle precipitation. The ultraviolet ionization by sunlight is
 152 strongly dependent on the time of day (day vs night), latitude (more ionization near
 153 the equator). The ionization due to particle precipitation, on the other hand, is highly

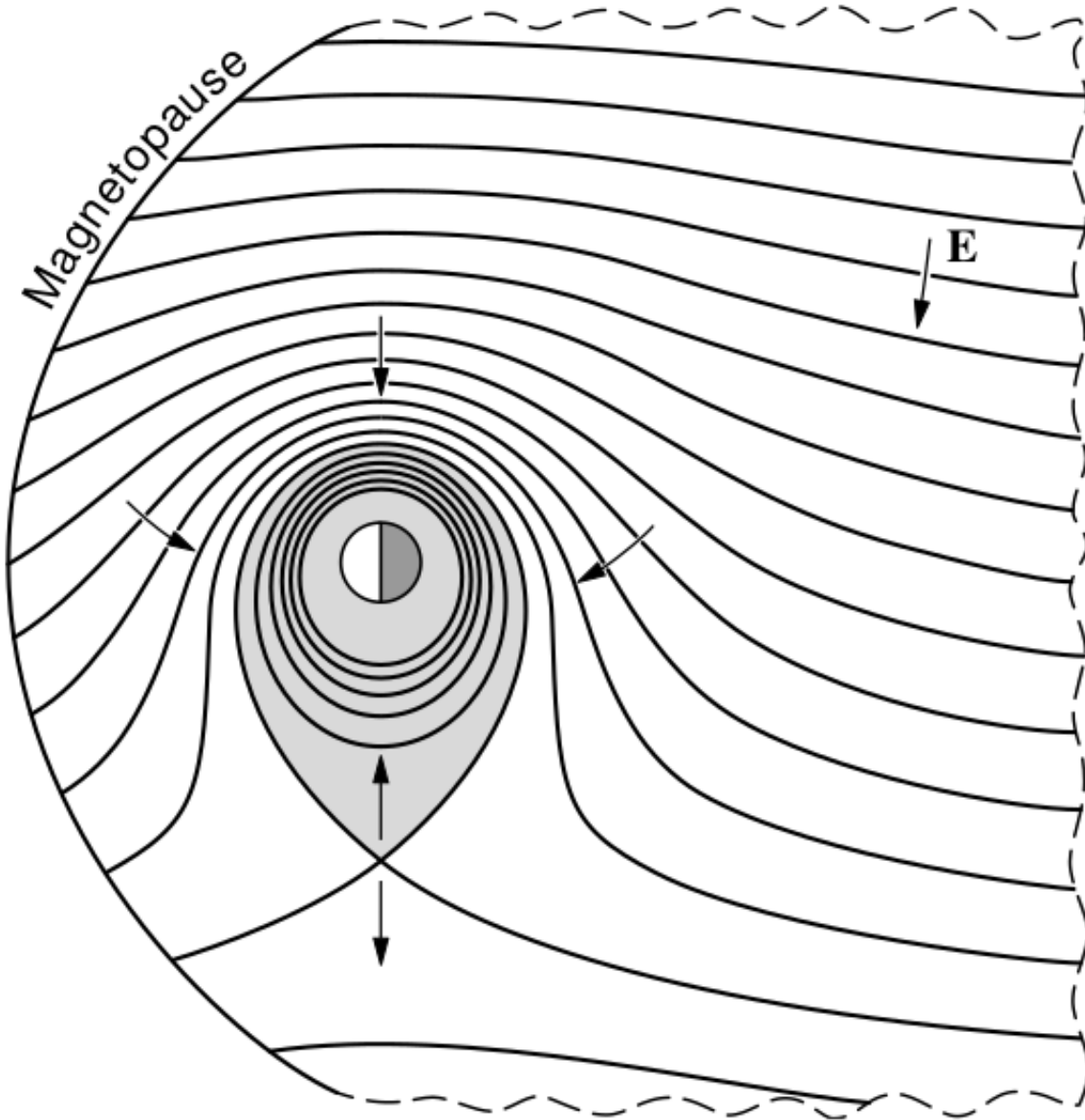


Figure 1.5: Equipotential lines and electric field arrows due to the superposition of the co-rotation and convection electric fields. Electrons in the shaded region execute closed orbits. Outside of the shaded regions the electrons are not trapped and will escape. The region separating the two regimes is called the Alfvén layer. Figure from Baumjohann and Treumann (1997).

¹⁵⁴ dependent on magnetospheric conditions, and mostly occurs at high latitudes.

¹⁵⁵ The outer boundary of the plasmasphere is the plasmapause which is typically
¹⁵⁶ identified as a steep radial gradient in plasma density from $\sim 10^3/\text{cm}^3$ to $\sim 1/\text{cm}^3$. As
¹⁵⁷ we will see throughout this dissertation, the location of the plasmapause is important
¹⁵⁸ to model (e.g. O'Brien and Moldwin, 2003) and understand since the plasma density
¹⁵⁹ strongly controls the efficiency of particle scattering (Horne et al., 2005).

¹⁶⁰ Ring Current The next higher energy population is the ring current. This
¹⁶¹ population consists of protons and electrons between tens and a few hundred keV
¹⁶² that drift around the Earth. The orbits of higher energy particles are not as effected
¹⁶³ by the convection and co-rotation electric field, rather they drift around the Earth
¹⁶⁴ due to gradient and curvature drifts. Since the direction of the drift is dependent on
¹⁶⁵ charge, protons drift west around the Earth and electrons drift East. This has the
¹⁶⁶ effect of creating a current around the Earth.

¹⁶⁷ The ring current generates a magnetic field which decreases the magnetic field
¹⁶⁸ strength on Earth's surface and increases it outside of the ring current. The decrease
¹⁶⁹ of Earth's magnetic field strength is readily observed by a system of ground-based
¹⁷⁰ magnetometers and is merged into a Disturbance Storm Time (DST) index. An
¹⁷¹ example of a DST index time series from a coronal mass ejection (CME) driven 2015
¹⁷² St. Patrick's Day storm is shown in Fig. 1.6. The ring current is sometimes first
¹⁷³ depleted and DST increases slightly (initial phase or sudden storm commencement).
¹⁷⁴ Then the ring current is rapidly built up during which DST rapidly decreases (main
¹⁷⁵ phase). Lastly the ring current gradually decays toward its equilibrium state over a
¹⁷⁶ period of a few days and DST increases towards 0 (recovery phase). The DST index
¹⁷⁷ along with other indicies are readily used by the space physics community to quantify
¹⁷⁸ the global state of the magnetosphere.

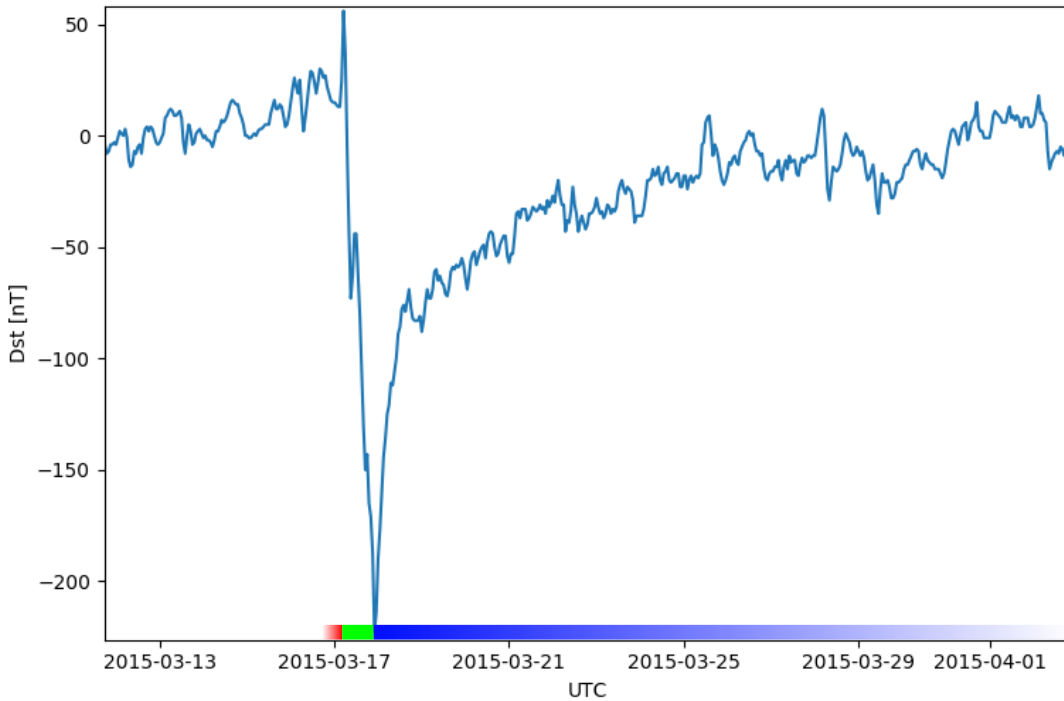


Figure 1.6: The DST index during the St. Patrick's Day 2015 storm. This storm was caused by a coronal mass ejection on March 15th, 2015. The storm phases are: initial phase, main phase, and recovery phase. The initial phase occurred when the Dst peaked at $+50$ nT on March 17th during which the ring current was eroded by the coronal mass ejection during the interval shown by the red bar. Then the rapid decrease to ≈ -200 nT was during the main phase where many injections from the magnetotail pumped up the ring current which reduced Earth's magnetic field strength at the ground and is shown with the green bar. Lastly, the recovery phase lasted from March 18th to approximately March 29th during which the ring current particles were lost and the ring current returned to its equilibrium state. The recovery phase is shown with the blue bar.

The Earth's Electron Radiation Belts

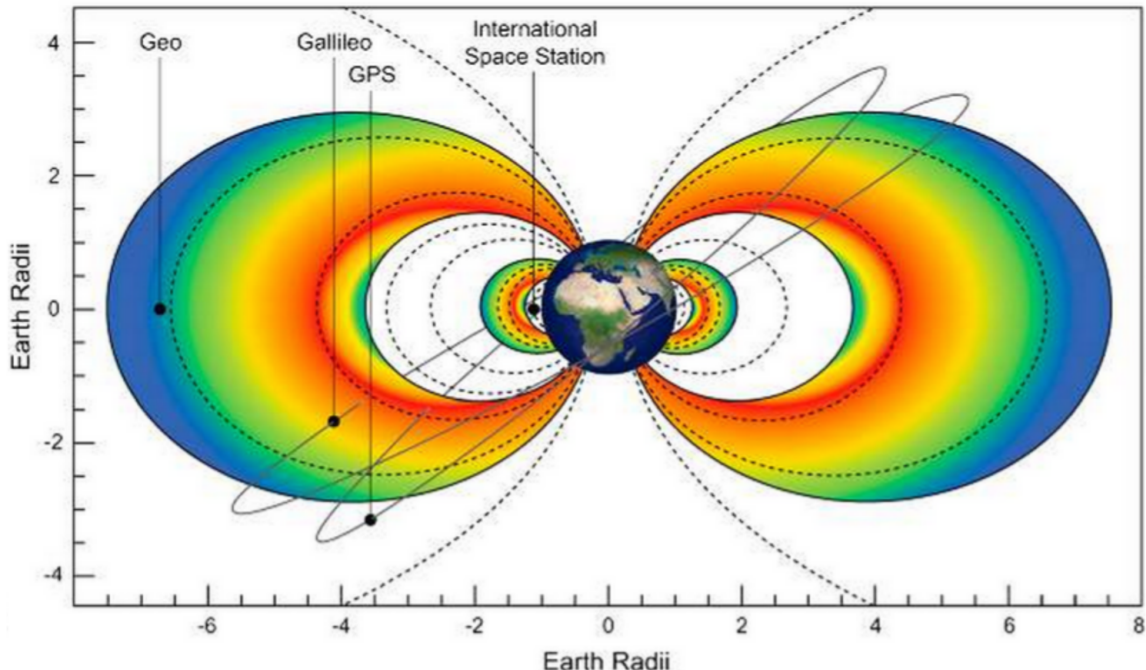


Figure 1.7: The two radiation belts with the locations of various satellites and orbits. Figure from (Horne et al., 2013).

179 Radiation Belts The highest energy particle populations are in the Van Allen
 180 radiation belts. These belts were discovered by Van Allen (1959) and Vernov and
 181 Chudakov (1960) during the Cold War and are a pair of toroidally shaped populations
 182 of trapped electrons and protons usually within to $L < 8$ and are shown in Fig. 1.7.
 183 Their quiescent toroidal shape is similar to the shape of the plasmasphere and ring
 184 current and is a result of Earth's dipole magnetic field and the conservation of the
 185 three adiabatic invariants discussed in section 1.

186 The inner radiation belt is extremely stable on time periods of years, extends
 187 to $L \approx 2$, and mainly consists of protons with energies between MeV and GeV and
 188 electrons with energies up to ≈ 1 MeV (Claudepierre et al., 2019). The source of
 189 inner radiation belt protons is believed to be due to cosmic-ray albedo neutron decay

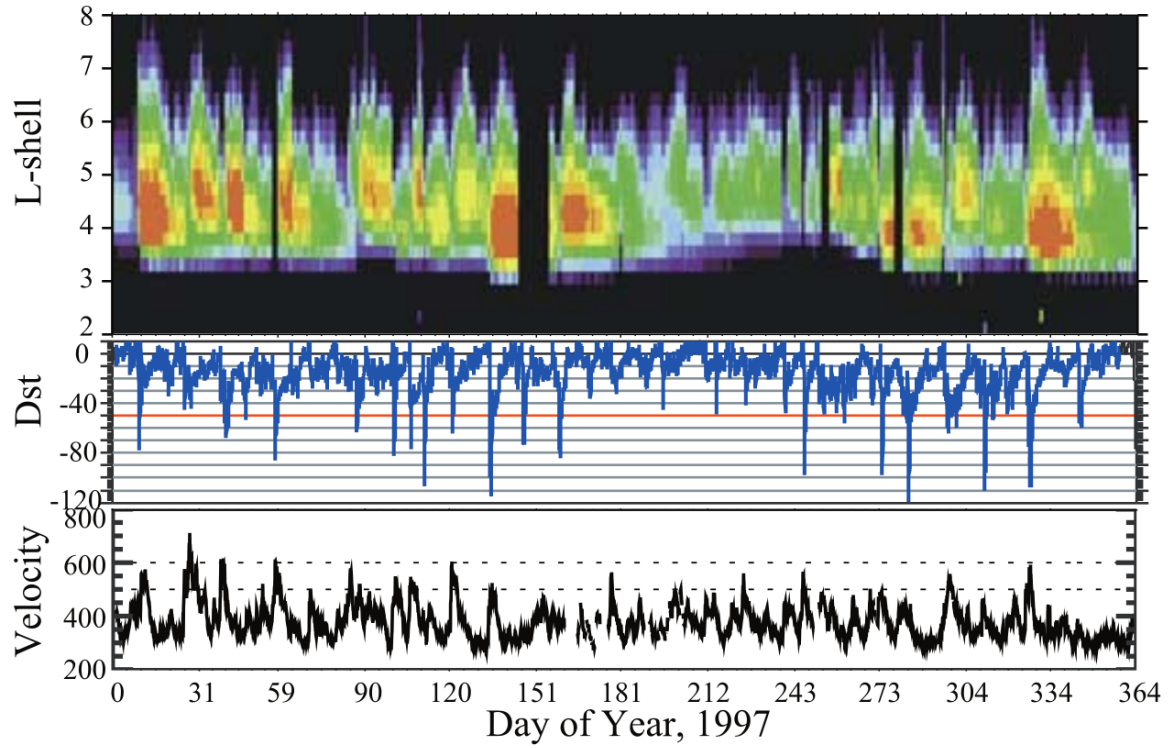


Figure 1.8: The dynamics of the outer radiation belt in 1997 from the POLAR satellite. Top panel shows the 1.2-2.4 MeV electron flux as a function of L and 1997 day of year. The middle panel shows the DST index, and bottom panel shows the solar wind velocity. Figure from (Reeves et al., 2003).

(e.g. Li et al., 2017) and inward radial diffusion for electrons (e.g. O'Brien et al., 2016). The gap between the inner and outer radiation belt is called the slot, which is believed to be due to hiss waves inside the plasmasphere (described below) scattering particles into the atmosphere (e.g. Breneman et al., 2015; Lyons and Thorne, 1973).

The outer radiation belt, on the other hand is much more dynamic and consists of mainly electrons of energies up to a few MeV. The outer belt's spatial extent is highly variable e.g. see Fig. 1.8, and is typically observed at $4 < L < 8$. Since the outer radiation belt contains a dynamic population of energetic particles that pose a threat to human and technological presence in Earth's atmosphere and space, decades of research has been undertaken to understand and predict the outer radiation belt particles, waves, and wave-particle interactions. The dynamics of the outer radiation belt can be understood by considering various competing acceleration and loss mechanisms which will be described in the following sections.

203

Radiation Belt Particle Sources and Sinks

Adiabatic Heating

One of the particle heating and transport mechanisms arises from the Earthward convection of particles. The conservation of J_1 implies that the initial and final v_\perp depends on the change in the magnetic field amplitude

$$\frac{v_{\perp i}^2}{B_i} = \frac{v_{\perp f}^2}{B_f}. \quad (1.12)$$

As a particle convects Earthward, $B_f > B_i$ thus v_\perp must increase. The dipole magnetic field amplitude can be written as

$$B(L, \theta) = \frac{31.2 \mu\text{T}}{L^3} \sqrt{1 + 3 \cos^2 \theta} \quad (1.13)$$

²¹⁰ which implies that

$$\frac{v_{\perp f}^2}{v_{\perp i}^2} = \left(\frac{L_i}{L_f}\right)^3. \quad (1.14)$$

²¹¹ .

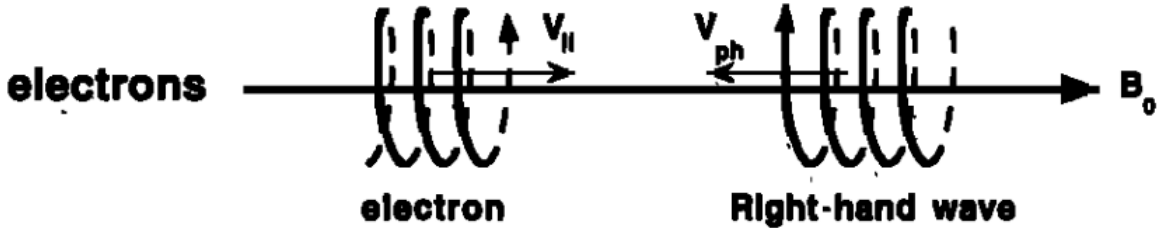
²¹² In addition, as the particle convects Earthward the distance between the
²¹³ particle's mirror points decrease. If J_2 is conserved, the shrinking bounce path implies
²¹⁴ that $v_{||}$ must increase by

$$\frac{v_{|| f}^2}{v_{|| i}^2} = \left(\frac{L_i}{L_f}\right)^k \quad (1.15)$$

²¹⁵ where k ranges from 2 for equatorial pitch angles, $\alpha_{eq} = 0^\circ$, to 2.5 for $\alpha_{eq} = 90^\circ$
²¹⁶ (Baumjohann and Treumann, 1997). Since the rate of adiabatic heating is greater in
²¹⁷ the perpendicular direction than heating in the parallel direction, an initially isotropic
²¹⁸ particle distribution will become anisotropic during its convection. These isotropic
²¹⁹ particles can then become unstable to wave growth and generate waves in order to
²²⁰ reach equilibrium.

²²¹ Wave Resonance Heating

²²² Another mechanism that heats particles is due to particles resonating with
²²³ plasma waves. A few of the electromagnetic wave modes responsible for particle
²²⁴ acceleration (and deceleration) relevant to radiation belt dynamics are hiss, whistler
²²⁵ mode chorus (chorus), and electromagnetic ion cyclotron (EMIC) waves. These waves
²²⁶ are created by the loss cone instability that driven by an anisotropy of electrons
²²⁷ for chorus waves, and protons for EMIC waves. The level of anisotropy can be
²²⁸ quantified by the ratio of the perpendicular to parallel particle temperatures ($T_{\perp}/T_{||}$).
²²⁹ A particle distribution is unstable when $T_{\perp}/T_{||} > 1$ which facilitates wave growth.



$$\omega + k_{\parallel} v_{\parallel} = \Omega^-$$

Figure 1.9: The trajectories of an electron and a right-hand circularly polarized wave during a cyclotron resonance. The electron's v_{\parallel} and the wave's k_{\parallel} are in opposite directions such that the wave's frequency is Doppler shifted to an integer multiple of the electron cyclotron frequency. Figure from (Tsurutani and Lakhina, 1997).

230 Since electrons gyrate in a right-handed sense, the chorus waves also tend to be right
 231 hand circularly polarized (Tsurutani and Lakhina, 1997). The same argument applies
 232 to protons and left hand circularly polarized EMIC waves as well.

233 These circularly polarized waves can resonate with electrons and/or protons
 234 when their combined motion results in a static \vec{E} . One example of a resonance
 235 between a right hand circularly polarized wave and an electron is shown in Fig. 1.21
 236 and is termed the cyclotron resonance. An electron's v_{\parallel} and the wave's parallel wave
 237 vector, k_{\parallel} are in opposite directions such that the wave frequency ω is Doppler shifted
 238 to an integer multiple of the Ω_e at which point the electron feels a static electric
 239 field and is accelerated or decelerated. This acceleration happens when a resonance
 240 condition is satisfied between a wave and a particle for which we will now derive an
 241 illustrative toy model.

242 Assume a uniform magnetic field $\vec{B} = B_0 \hat{z}$ with a parallel propagating ($k = k \hat{z}$),
 243 right-hand circularly polarized wave. The wave's electric field as a function of position
 244 and time can be written as

$$\vec{E} = E_0 (\cos(\omega t - kz) \hat{x} + \sin(\omega t - kz) \hat{y}) \quad (1.16)$$

which is more clearly expressed by taking the dot product to find \vec{E} in the $\hat{\theta}$ direction

$$E_\theta = \vec{E} \times \hat{\theta} = E_0 \cos(\omega t - kz + \theta). \quad (1.17)$$

²⁴⁵ Now assume that the electron is traveling in the $-\hat{z}$ direction with a velocity $\vec{v} = -v_0 \hat{z}$
²⁴⁶ so its time dependent position along \hat{z} is

$$z(t) = -v_0 t \quad (1.18)$$

²⁴⁷ and gyrophase is

$$\theta(t) = -\Omega t + \theta(0) \quad (1.19)$$

²⁴⁸ where the first negative sign comes from the electron's negative charge. Now we put
²⁴⁹ this all together and express the electric field and the force that the electron will
²⁵⁰ experience

$$m \frac{dv_\theta}{dt} = qE_\theta = qE_0 \sin((\omega + kv_0 - \Omega)t + \theta(0)). \quad (1.20)$$

²⁵¹ This is a relatively complex expression, but when the time dependent component,

$$\omega + kv_0 - \Omega = 0, \quad (1.21)$$

²⁵² the electron will be in a static electric field which will accelerate or decelerate the
²⁵³ electron depending on θ_0 , the phase between the wave and the electron. **Show Bortnik
²⁵⁴ 2008 plot?** The expression in Eq. 1.21 is commonly referred to as the resonance

255 condition and is more generally written as

$$\omega - k_{||}v_{||} = \frac{n\Omega_e}{\gamma} \quad (1.22)$$

256 where n is the resonance order, and γ is the relativistic correction (e.g. Millan and
 257 Thorne, 2007). In the case of the cyclotron resonance, $\omega \approx \Omega_e$ thus J_1 is violated.
 258 Since J_1 is violated, J_2 and J_3 are also violated since the conditions required to
 259 violate J_2 and J_3 are less stringent than J_1 . It is important to remember that along
 260 the particle's orbit it will encounter and experience the effects of many waves along
 261 its orbit. The typical MLT extent of a handful of waves that are capable of resonating
 262 with radiation belt electrons are shown in Fig. 1.10.

263 Particle Losses

264 Now that we have seen two general mechanisms with which particles are
 265 accelerated and transported in the magnetosphere, we will now consider a few
 266 specific mechanisms with which particles are lost to the atmosphere or the solar
 267 wind. One particle loss mechanism into the solar wind is magnetopause shadowing
 268 (e.g. Ukhorskiy et al., 2006). Particles are sometimes lost when the ring current is
 269 strengthened and Earth's magnetic field strength is increased outside of the ring
 270 current (and reduced on Earth's surface). If the time scale of the ring current
 271 strengthening is slower than a particle drift, J_3 is conserved. Then in order to
 272 conserve J_3 while the magnetic field strength is increased, the particle's drift shell
 273 must move outward to conserve the magnetic flux contained by the drift shell. Then
 274 if the particle's drift shell expands to the point that it crosses the magnetopause, the
 275 particle will be lost to the solar wind.

276 Another particle loss (and acceleration) mechanism is driven by ultra low
 277 frequency (ULF) waves and is called radial diffusion. Radial diffusion is the transport

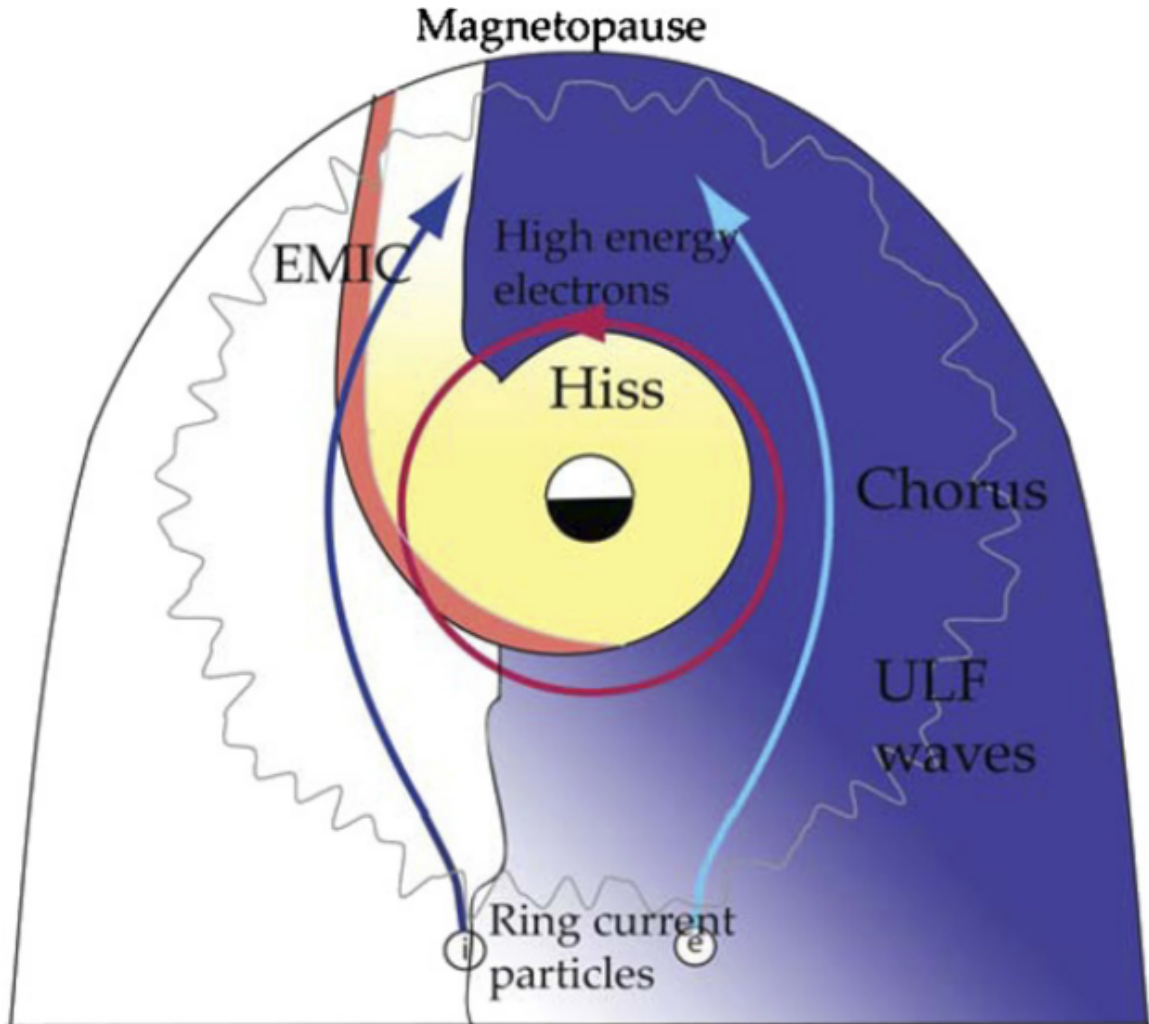


Figure 1.10: Various wave modes in the magnetosphere. Ultra low frequency waves occur through the magnetosphere. Chorus waves are typically observed in the 0-12 midnight-dawn region. EMIC waves are typically observed in the dusk MLT sector. Hiss waves are observed inside the plasmasphere. Figure from Millan and Thorne (2007).

278 of particles from high to low phase space density, f . If the transport is radially inward,
 279 particles will appear to be accelerated. On the other hand, radially outward radial
 280 diffusion can transport particles through the magnetopause where they will be lost
 281 to the solar wind. Reeves et al. (2013) investigated the driver of particle acceleration
 282 during the October 2012 storm and observationally found that inward radial diffusion
 283 was not dominant, rather local acceleration via wave-resonance heating (i.e. particle
 284 diffusion in pitch angle and energy which will be described below) appeared to be the
 285 dominant acceleration mechanism.

286 The loss mechanism central to this dissertation is pitch angle and energy
 287 scattering of electrons by waves. Some of the waves that scatter electrons in energy
 288 and pitch angle in the inner magnetosphere are: plasmaspheric hiss (e.g. Breneman
 289 et al., 2015; O'Brien et al., 2014), EMIC waves (e.g. Capannolo et al., 2019; Hendry
 290 et al., 2017), and chorus waves (e.g. Breneman et al., 2017; Kasahara et al., 2018;
 291 Ozaki et al., 2019). These wave-particle interactions occur when the resonance
 292 condition in Eq. 1.22 is satisfied at which point the particle's energy and α is modified
 293 by the wave. More details regarding the theory of pitch angle and energy diffusion is
 294 given in Chapter X. If the wave changes α towards 0 such that $\alpha < \alpha_{LC}$, the particle's
 295 mirror point lowers to less than 100 km altitude where the particle can be lost due
 296 collisions with air. One manifestation of pitch angle scattering of particles into the
 297 loss cone are microbursts: a sub-second duraion impulse of electrons.

298

Microbursts

299 Microbursts were first found in high altitude balloon measurements of bremsstrahlung
 300 X-rays emitted by microburst electrons impacting the atmosphere by Anderson
 301 and Milton (1964). In the following years, numerous balloon flights expanded our
 302 knowledge of non-relativistic microbursts (relativistic microbursts have not yet been

303 observed by high altitude balloons) by quantifying the microburst spatial extent,
 304 temporal width, occurrence frequency, extent in L and MLT, and their source (a
 305 local plasma instability vs. a propagating disturbance in the magnetosphere) (e.g.
 306 Barcus et al., 1966; Brown et al., 1965; Parks, 1967; Trefall et al., 1966). Since then,
 307 non-relativistic and relativistic (> 500 keV) microbursts electrons have been directly
 308 observed in LEO with spacecraft including the Solar Anomalous and Magnetospheric
 309 Particle Explorer (SAMPEX) (e.g. Blake et al., 1996; Blum et al., 2015; Douma et al.,
 310 2019, 2017; Greeley et al., 2019; Lorentzen et al., 2001a,b; Nakamura et al., 1995, 2000;
 311 O'Brien et al., 2004, 2003), Montana State University's (MSU) Focused Investigation
 312 of Relativistic Electron Bursts: Intensity, Range, and Dynamics II (FIREBIRD-II)
 313 (Anderson et al., 2017; Breneman et al., 2017; Crew et al., 2016; Klumpar et al.,
 314 2015; Spence et al., 2012), and Science Technologies Satellite (STSAT-I) (e.g. Lee
 315 et al., 2012, 2005). An example microburst time series is shown in Fig. 1.11 and was
 316 observed by the FIREBIRD-II CubeSats. The prominent features of the example
 317 microbursts in Fig. 1.11 are their < 1 second duration, half order of magnitude
 318 increase in count rate above the falling background, and their approximately 200-800
 319 keV energy extent.

320 Microbursts are observed on magnetic field footprints that are connected to the
 321 outer radiation belt (approximately $4 < L < 8$), and are predominately observed in
 322 the 0-12 MLT sector with an elevated occurrence frequency during magnetospherically
 323 disturbed times as shown in Fig. 1.12 (e.g. Douma et al., 2017). O'Brien et al. (2003)
 324 used SAMPEX relativistic electron data and found that microbursts predominately
 325 occur during the main phase of storms, with a heightened occurrence rate during the
 326 recovery phase. Microburst occurrence rates also appear to be higher during high
 327 solar wind velocity events e.g. from co-rotating interaction regions (Greeley et al.,
 328 2019; O'Brien et al., 2003).

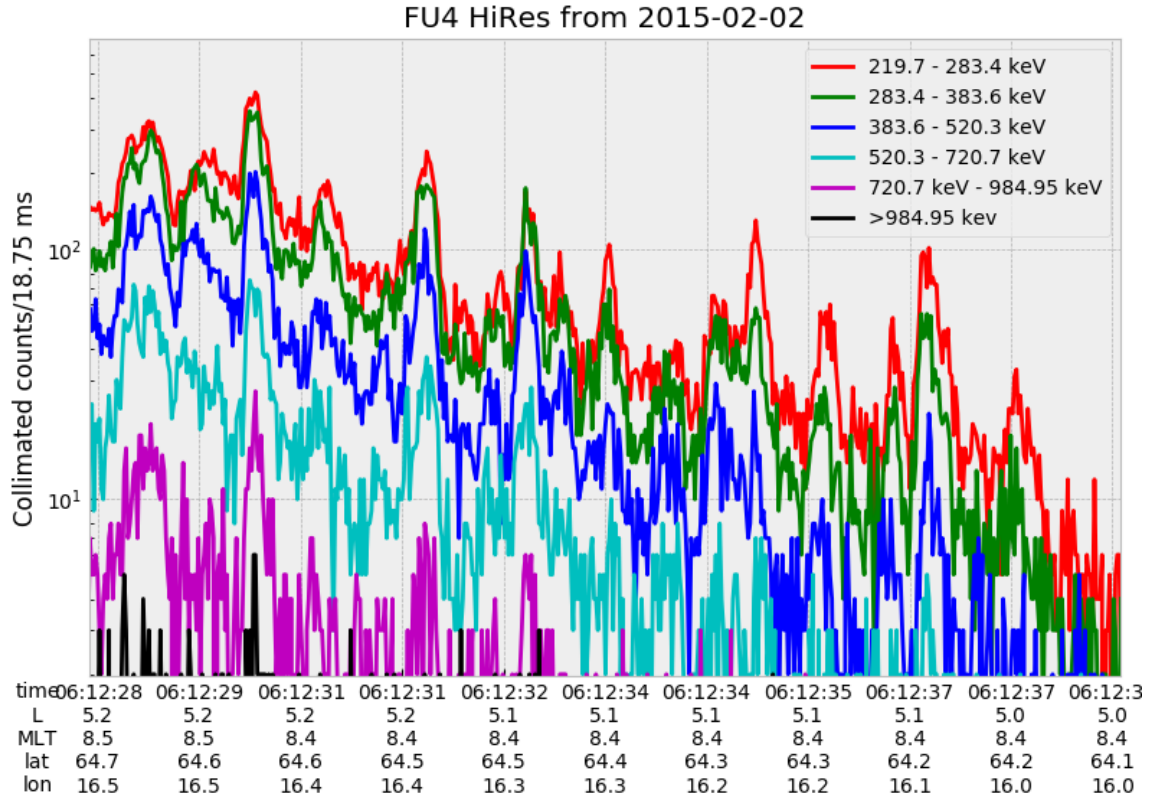


Figure 1.11: An example train of microbursts observed by FIREBIRD-II unit 4 on February 2nd, 2015. The colored curves show the differential energy channel count rates in six channels from ≈ 200 keV to greater than 1 MeV. The x-axis labels show auxiliary information such as time of observation and the spacecraft position in L, MLT, latitude and longitude coordinates.

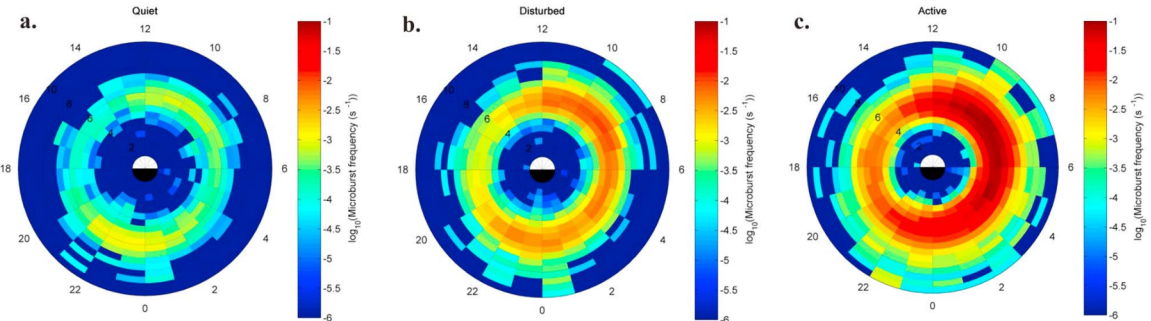


Figure 1.12: Relativistic ($> 1\text{MeV}$) distribution of microburst occurrence rates as a function of L and MLT. The three panels show the microburst occurrence rate dependence on geomagnetic activity, parameterized by the auroral electrojet (AE) index for (a) $\text{AE} < 100 \text{ nT}$, (b) $100 < \text{AE} < 300 \text{ nT}$ and (c) $\text{AE} > 300 \text{ nT}$. Figure from Douma et al. (2017).

329 The impact of microbursts on atmospheric chemistry has been estimated to be
 330 significant. Relativistic microburst electrons impacting the atmosphere are ionized at
 331 $< 100 \text{ km}$ altitudes, with higher energy electrons penetrating closer to the surface.
 332 The resulting chemical reaction of microburst electrons impacting the atmosphere
 333 produces odd hydrogen HO_x and odd nitrogen NO_x molecules. These molecules are
 334 partially responsible for destroying ozone (O_3). Seppälä et al. (2018) modeled a six
 335 hour relativistic microburst storm and found that the mesospheric ozone was reduced
 336 by 7 – 12% in the summer months and 12 – 20% in the winter months.

337 Furthermore, microbursts have also been estimated to have a significant impact
 338 on the outer radiation belt electrons. Radiation belt electron loss due to microbursts
 339 has been estimated to be on the order of a day (Breneman et al., 2017; Douma
 340 et al., 2019; Lorentzen et al., 2001b; O'Brien et al., 2004; Thorne et al., 2005).

341 The wave-particle interactions responsible for generating microbursts are also
 342 believed to accelerate electrons in the radiation belts. As mentioned earlier, when
 343 an electron is in resonance with a wave, energy is exchanged with the wave and
 344 the electron is either accelerated or decelerated. The signature of wave-particle

345 acceleration been observed for radiation belt electrons (e.g. Horne et al., 2005;
 346 Meredith et al., 2002; Reeves et al., 2013). O'Brien et al. (2003) presented evidence
 347 that enhancements in chorus waves, microbursts, and radiation belt electrons are
 348 related. O'Brien et al. (2003) proposed an explanation where microburst precipitation
 349 is a side effect of electron acceleration due to chorus waves. The widely used
 350 theoretical framework to model interactions between electrons and chorus waves is
 351 quasi-linear diffusion (e.g. Horne et al., 2005; Meredith et al., 2002; Summers, 2005;
 352 Summers et al., 1998; Thorne et al., 2005; Walker, 1993) which is derived in Chapter
 353 ???. Qualitatively, when a particle is resonant with a wave it can be transported in
 354 pitch angle towards the loss cone and lose energy to the wave. In contrast, if the
 355 particle is transported away from the loss cone, it gains energy from the wave.

356 The range of observed microburst energies range from a few tens of keV (e.g.
 357 Datta et al., 1997; Parks, 1967) to greater than 1 MeV (e.g. Blake et al., 1996; Greeley
 358 et al., 2019). The microburst electron flux (J) falls off in energy, and the microburst
 359 energy spectra is typically well fit to a decaying exponential

$$J(E) = J_0 e^{-E/E_0} \quad (1.23)$$

360 where J_0 is the flux at 0 keV (unphysical free parameter) and E_0 quantifies the
 361 efficiency of the scattering mechanism in energy (.e.g Datta et al., 1997; Lee et al.,
 362 2005; Parks, 1967). A small E_0 suggests that mostly low energy particles are scattered
 363 and a high E_0 suggests that the scattering mechanism scatters low and high energy
 364 electrons. Reality is a bit more messy and a high E_0 may be a signature of a scattering
 365 mechanism preferential to high energy electrons, but is hidden by the convolution of
 366 the source particles available to be scattered (typically with a falling energy spectrum)
 367 and the energy-dependent scattering efficiency.

368 The short duration of microbursts observed by a single LEO satellite has an
 369 ambiguity when interpreting what is exactly a microburst. The two possible realities
 370 are: a microburst is very small and spatially stationary so that the LEO spacecraft
 371 passes through it in less than a second. Alternatively, microbursts are spatially large
 372 with a short duration such that the microburst passes by the spacecraft in a fraction
 373 of a second. There are a few ways to distinguish between the two possible realities,
 374 and each one has a unique set of advantages.

375 A high altitude balloon provides essentially a stationary view of the precipitating
 376 particles under the radiation belt footprints so a short-lived, temporal microburst can
 377 be unambiguously identified. Spatial structures, on the other hand, are difficult to
 378 identify because a balloon is essentially still on drift timescales.

379 Multi-spacecraft missions are an alternate solution which can determine if a
 380 microburst-like feature is spatial or temporal. As will be shown in this dissertation,
 381 if a microburst is observed simultaneously by two spacecraft then it is temporal and
 382 has a size greater than the spacecraft separation. On the contrary, if two spacecraft
 383 observe a microburst-like feature at different times, but at the same location, then
 384 the feature is spatial and may be a curtain (Blake and O'Brien, 2016). Both balloon
 385 and multi-spacecraft observational methods have a unique set of strengths, and this
 386 dissertation takes the multi-spacecraft approach to identify and study microbursts.

387 Scope of Research

388 This dissertation furthers our understanding of the microburst scattering
 389 mechanism by observing the scattering directly, and measuring the microburst sizes
 390 and comparing them to the size of waves near the magnetic equator where those
 391 electrons could have been scattered. Chapter ?? describes a microburst scattering
 392 event observed by NASA's Van Allen Probes which was studied in the theoretic

393 framework of pitch angle and energy diffusion. The following two chapters will then
394 study the size of microbursts. Chapter ?? describes a bouncing packet microburst
395 observation made by MSU’s FIREBIRD-II mission where the microburst’s lower
396 bound longitudinal and latitudinal sizes were estimated. Then Chapter ?? expands
397 the case study from Ch. ?? to a statistical study of microburst sizes using The
398 Aerospace Corporation’s AeroCube-6 (AC6) CubeSats. In this study, a Monte Carlo
399 and analytic microburst size models were developed to account for the compounding
400 effects of random microburst sizes and locations. Lastly, Chapter ?? will summarize
401 the dissertation work and make concluding remarks regarding outstanding questions
402 in microburst physics.

Bibliography

- 404 Anderson, B., Shekhar, S., Millan, R., Crew, A., Spence, H., Klumpar, D., Blake, J.,
 405 O'Brien, T., and Turner, D. (2017). Spatial scale and duration of one microburst
 406 region on 13 August 2015. *Journal of Geophysical Research: Space Physics*.
- 407 Anderson, K. A. and Milton, D. W. (1964). Balloon observations of X rays in the
 408 auroral zone: 3. High time resolution studies. *Journal of Geophysical Research*,
 409 69(21):4457–4479.
- 410 Barcus, J., Brown, R., and Rosenberg, T. (1966). Spatial and temporal character of
 411 fast variations in auroral-zone x rays. *Journal of Geophysical Research*, 71(1):125–
 412 141.
- 413 Baumjohann, W. and Treumann, R. A. (1997). *Basic space plasma physics*. World
 414 Scientific.
- 415 Blake, J.,Looper, M., Baker, D., Nakamura, R., Klecker, B., and Hovestadt, D.
 416 (1996). New high temporal and spatial resolution measurements by sampex of the
 417 precipitation of relativistic electrons. *Advances in Space Research*, 18(8):171 – 186.
- 418 Blake, J. B. and O'Brien, T. P. (2016). Observations of small-scale latitudinal
 419 structure in energetic electron precipitation. *Journal of Geophysical Research: Space
 420 Physics*, 121(4):3031–3035. 2015JA021815.
- 421 Blum, L., Li, X., and Denton, M. (2015). Rapid MeV electron precipitation as
 422 observed by SAMPEX/HILT during high-speed stream-driven storms. *Journal of
 423 Geophysical Research: Space Physics*, 120(5):3783–3794. 2014JA020633.
- 424 Breneman, A., Crew, A., Sample, J., Klumpar, D., Johnson, A., Agapitov, O.,
 425 Shumko, M., Turner, D., Santolik, O., Wygant, J., et al. (2017). Observations
 426 directly linking relativistic electron microbursts to whistler mode chorus: Van allen
 427 probes and FIREBIRD II. *Geophysical Research Letters*.
- 428 Breneman, A. W., Halford, A., Millan, R., McCarthy, M., Fennell, J., Sample, J.,
 429 Woodger, L., Hospodarsky, G., Wygant, J. R., Cattell, C. A., et al. (2015). Global-
 430 scale coherence modulation of radiation-belt electron loss from plasmaspheric hiss.
 431 *Nature*, 523(7559):193.
- 432 Brown, R., Barcus, J., and Parsons, N. (1965). Balloon observations of auroral zone
 433 x rays in conjugate regions. 2. microbursts and pulsations. *Journal of Geophysical
 434 Research (U.S.)*.
- 435 Capannolo, L., Li, W., Ma, Q., Shen, X.-C., Zhang, X.-J., Redmon, R., Rodriguez,
 436 J., Engebretson, M., Kletzing, C., Kurth, W., et al. (2019). Energetic electron
 437 precipitation: multi-event analysis of its spatial extent during emic wave activity.
 438 *Journal of Geophysical Research: Space Physics*.

- 439 Claudepierre, S., O'Brien, T.,Looper, M., Blake, J., Fennell, J., Roeder, J.,
 440 Clemmons, J., Mazur, J., Turner, D., Reeves, G., et al. (2019). A revised look
 441 at relativistic electrons in the earth's inner radiation zone and slot region. *Journal*
 442 of *Geophysical Research: Space Physics*, 124(2):934–951.
- 443 Crew, A. B., Spence, H. E., Blake, J. B., Klumpar, D. M., Larsen, B. A., O'Brien,
 444 T. P., Driscoll, S., Handley, M., Legere, J., Longworth, S., Mashburn, K.,
 445 Mosleh, E., Ryhajlo, N., Smith, S., Springer, L., and Widholm, M. (2016). First
 446 multipoint in situ observations of electron microbursts: Initial results from the
 447 NSF FIREBIRD II mission. *Journal of Geophysical Research: Space Physics*,
 448 121(6):5272–5283. 2016JA022485.
- 449 Datta, S., Skoug, R., McCarthy, M., and Parks, G. (1997). Modeling of microburst
 450 electron precipitation using pitch angle diffusion theory. *Journal of Geophysical*
 451 *Research: Space Physics*, 102(A8):17325–17333.
- 452 Douma, E., Rodger, C., Blum, L., O'Brien, T., Clilverd, M., and Blake, J. (2019).
 453 Characteristics of relativistic microburst intensity from sampex observations.
 454 *Journal of Geophysical Research: Space Physics*.
- 455 Douma, E., Rodger, C. J., Blum, L. W., and Clilverd, M. A. (2017). Occurrence
 456 characteristics of relativistic electron microbursts from SAMPEX observations.
 457 *Journal of Geophysical Research: Space Physics*, 122(8):8096–8107. 2017JA024067.
- 458 Eastwood, J., Hietala, H., Toth, G., Phan, T., and Fujimoto, M. (2015). What
 459 controls the structure and dynamics of earths magnetosphere? *Space Science*
 460 *Reviews*, 188(1-4):251–286.
- 461 Greeley, A., Kanekal, S., Baker, D., Klecker, B., and Schiller, Q. (2019). Quantifying
 462 the contribution of microbursts to global electron loss in the radiation belts. *Journal*
 463 of *Geophysical Research: Space Physics*.
- 464 Hendry, A. T., Rodger, C. J., and Clilverd, M. A. (2017). Evidence of sub-mev
 465 emic-driven electron precipitation. *Geophysical Research Letters*, 44(3):1210–1218.
- 466 Horne, R., Glauert, S., Meredith, N., Boscher, D., Maget, V., Heynderickx, D., and
 467 Pitchford, D. (2013). Space weather impacts on satellites and forecasting the earth's
 468 electron radiation belts with spacecast. *Space Weather*, 11(4):169–186.
- 469 Horne, R. B., Thorne, R. M., Shprits, Y. Y., Meredith, N. P., Glauert, S. A., Smith,
 470 A. J., Kanekal, S. G., Baker, D. N., Engebretson, M. J., Posch, J. L., et al.
 471 (2005). Wave acceleration of electrons in the van allen radiation belts. *Nature*,
 472 437(7056):227.
- 473 Kasahara, S., Miyoshi, Y., Yokota, S., Mitani, T., Kasahara, Y., Matsuda, S.,
 474 Kumamoto, A., Matsuoka, A., Kazama, Y., Frey, H., et al. (2018). Pulsating
 475 aurora from electron scattering by chorus waves. *Nature*, 554(7692):337.

- 476 Klumpar, D., Springer, L., Mosleh, E., Mashburn, K., Berardinelli, S., Gunderson,
 477 A., Handly, M., Ryhajlo, N., Spence, H., Smith, S., Legere, J., Widholm, M.,
 478 Longworth, S., Crew, A., Larsen, B., Blake, J., and Walmsley, N. (2015). Flight
 479 system technologies enabling the twin-cubesat firebird-ii scientific mission.
- 480 Lee, J. J., Parks, G. K., Lee, E., Tsurutani, B. T., Hwang, J., Cho, K. S., Kim, K.-H.,
 481 Park, Y. D., Min, K. W., and McCarthy, M. P. (2012). Anisotropic pitch angle
 482 distribution of 100 keV microburst electrons in the loss cone: measurements from
 483 STSAT-1. *Annales Geophysicae*, 30(11):1567–1573.
- 484 Lee, J.-J., Parks, G. K., Min, K. W., Kim, H. J., Park, J., Hwang, J., McCarthy,
 485 M. P., Lee, E., Ryu, K. S., Lim, J. T., Sim, E. S., Lee, H. W., Kang, K. I., and
 486 Park, H. Y. (2005). Energy spectra of 170–360 keV electron microbursts measured
 487 by the korean STSAT-1. *Geophysical Research Letters*, 32(13). L13106.
- 488 Li, X., Selesnick, R., Schiller, Q., Zhang, K., Zhao, H., Baker, D. N., and Temerin,
 489 M. A. (2017). Measurement of electrons from albedo neutron decay and neutron
 490 density in near-earth space. *Nature*, 552(7685):382.
- 491 Lorentzen, K. R., Blake, J. B., Inan, U. S., and Bortnik, J. (2001a). Observations
 492 of relativistic electron microbursts in association with VLF chorus. *Journal of
 493 Geophysical Research: Space Physics*, 106(A4):6017–6027.
- 494 Lorentzen, K. R.,Looper, M. D., and Blake, J. B. (2001b). Relativistic electron
 495 microbursts during the GEM storms. *Geophysical Research Letters*, 28(13):2573–
 496 2576.
- 497 Lyons, L. R. and Thorne, R. M. (1973). Equilibrium structure of radiation belt
 498 electrons. *Journal of Geophysical Research*, 78(13):2142–2149.
- 499 Meredith, N., Horne, R., Summers, D., Thorne, R., Iles, R., Heynderickx, D., and
 500 Anderson, R. (2002). Evidence for acceleration of outer zone electrons to relativistic
 501 energies by whistler mode chorus. In *Annales Geophysicae*, volume 20, pages 967–
 502 979.
- 503 Millan, R. and Thorne, R. (2007). Review of radiation belt relativistic electron losses.
 504 *Journal of Atmospheric and Solar-Terrestrial Physics*, 69(3):362 – 377.
- 505 Nakamura, R., Baker, D. N., Blake, J. B., Kanekal, S., Klecker, B., and Hovestadt,
 506 D. (1995). Relativistic electron precipitation enhancements near the outer edge of
 507 the radiation belt. *Geophysical Research Letters*, 22(9):1129–1132.
- 508 Nakamura, R., Isowa, M., Kamide, Y., Baker, D., Blake, J., and Looper, M. (2000).
 509 Observations of relativistic electron microbursts in association with VLF chorus.
 510 *J. Geophys. Res.*, 105:15875–15885.

- 511 O'Brien, T., Claudepierre, S., Blake, J., Fennell, J. F., Clemons, J., Roeder, J.,
 512 Spence, H. E., Reeves, G., and Baker, D. (2014). An empirically observed pitch-
 513 angle diffusion eigenmode in the earth's electron belt near $l^*= 5.0$. *Geophysical*
 514 *Research Letters*, 41(2):251–258.
- 515 O'Brien, T., Claudepierre, S., Guild, T., Fennell, J., Turner, D., Blake, J., Clemons,
 516 J., and Roeder, J. (2016). Inner zone and slot electron radial diffusion revisited.
 517 *Geophysical Research Letters*, 43(14):7301–7310.
- 518 O'Brien, T. and Moldwin, M. (2003). Empirical plasmapause models from magnetic
 519 indices. *Geophysical Research Letters*, 30(4).
- 520 O'Brien, T. P.,Looper, M. D., and Blake, J. B. (2004). Quantification of relativistic
 521 electron microburst losses during the GEM storms. *Geophysical Research Letters*,
 522 31(4). L04802.
- 523 O'Brien, T. P., Lorentzen, K. R., Mann, I. R., Meredith, N. P., Blake, J. B., Fennell,
 524 J. F., Looper, M. D., Milling, D. K., and Anderson, R. R. (2003). Energization of
 525 relativistic electrons in the presence of ULF power and MeV microbursts: Evidence
 526 for dual ULF and VLF acceleration. *Journal of Geophysical Research: Space*
 527 *Physics*, 108(A8).
- 528 Ozaki, M., Miyoshi, Y., Shiokawa, K., Hosokawa, K., Oyama, S.-i., Kataoka, R.,
 529 Ebihara, Y., Ogawa, Y., Kasahara, Y., Yagitani, S., et al. (2019). Visualization of
 530 rapid electron precipitation via chorus element wave–particle interactions. *Nature*
 531 *communications*, 10(1):257.
- 532 Parks, G. K. (1967). Spatial characteristics of auroral-zone X-ray microbursts. *Journal*
 533 *of Geophysical Research*, 72(1):215–226.
- 534 Reeves, G., Spence, H. E., Henderson, M., Morley, S., Friedel, R., Funsten, H., Baker,
 535 D., Kanekal, S., Blake, J., Fennell, J., et al. (2013). Electron acceleration in the
 536 heart of the van allen radiation belts. *Science*, 341(6149):991–994.
- 537 Reeves, G. D., McAdams, K. L., Friedel, R. H. W., and O'Brien, T. P. (2003). Ac-
 538 celeration and loss of relativistic electrons during geomagnetic storms. *Geophysical*
 539 *Research Letters*, 30(10):n/a–n/a. 1529.
- 540 Schulz, M. and Lanzerotti, L. J. (1974). *Particle Diffusion in the Radiation Belts*.
 541 Springer.
- 542 Seppälä, A., Douma, E., Rodger, C., Verronen, P., Clilverd, M. A., and Bortnik, J.
 543 (2018). Relativistic electron microburst events: Modeling the atmospheric impact.
 544 *Geophysical Research Letters*, 45(2):1141–1147.

- 545 Spence, H. E., Blake, J. B., Crew, A. B., Driscoll, S., Klumpar, D. M., Larsen,
 546 B. A., Legere, J., Longworth, S., Mosleh, E., O'Brien, T. P., Smith, S., Springer,
 547 L., and Widholm, M. (2012). Focusing on size and energy dependence of electron
 548 microbursts from the van allen radiation belts. *Space Weather*, 10(11).
- 549 Summers, D. (2005). Quasi-linear diffusion coefficients for field-aligned electro-
 550 magnetic waves with applications to the magnetosphere. *Journal of Geophysical
 551 Research: Space Physics*, 110(A8):n/a–n/a. A08213.
- 552 Summers, D., Thorne, R. M., and Xiao, F. (1998). Relativistic theory of wave-particle
 553 resonant diffusion with application to electron acceleration in the magnetosphere.
 554 *Journal of Geophysical Research: Space Physics*, 103(A9):20487–20500.
- 555 Thorne, R. M., O'Brien, T. P., Shprits, Y. Y., Summers, D., and Horne, R. B. (2005).
 556 Timescale for MeV electron microburst loss during geomagnetic storms. *Journal
 557 of Geophysical Research: Space Physics*, 110(A9). A09202.
- 558 Trefall, H., Bjordal, J., Ullaland, S., and Stadsnes, J. (1966). On the extension of
 559 auroral-zone x-ray microbursts. *Journal of Atmospheric and Terrestrial Physics*,
 560 28(2):225–233.
- 561 Tsurutani, B. T. and Lakhina, G. S. (1997). Some basic concepts of wave-particle
 562 interactions in collisionless plasmas. *Reviews of Geophysics*, 35(4):491–501.
- 563 Ukhorskiy, A. Y., Anderson, B. J., Brandt, P. C., and Tsyganenko, N. A. (2006).
 564 Storm time evolution of the outer radiation belt: Transport and losses. *Journal of
 565 Geophysical Research: Space Physics*, 111(A11):n/a–n/a. A11S03.
- 566 Van Allen, J. A. (1959). The geomagnetically trapped corpuscular radiation. *Journal
 567 of Geophysical Research*, 64(11):1683–1689.
- 568 Vernov, S. and Chudakov, A. (1960). Investigation of radiation in outer space. In
 569 *International Cosmic Ray Conference*, volume 3, page 19.
- 570 Walker, A. D. M. (1993). *Plasma waves in the magnetosphere*, volume 24. Springer
 571 Science & Business Media.